# End-gas autoignition and knocking combustion of ammonia/hydrogen/air mixtures in a confined reactor

*Zhou Yu, Huangwei Zhang*[*]

*Department of Mechanical Engineering, National University of Singapore, 9 Engineering Drive 1, 117576, Singapore*

## HIGHLIGHTS

- Detailed simulations on end-gas knocking combustion are performed.
- Ammonia and hydrogen binary fuel blends with different ratios are considered.
- Different end-gas combustion modes are observed from parametric studies.
- Evolutions of thermochemical states in end-gas combustion are discussed.
- Knocking intensity and timing in ammonia/hydrogen blending fuel are studied.

## ARTICLE INFO

## ABSTRACT

End-gas autoignition and detonation development in ammonia/hydrogen/air mixtures in a confined reactor is studied through detailed numerical simulations, to understand the knocking characteristics under IC engine relevant conditions. One-dimensional planar confined chamber filled with ammonia/hydrogen/air mixtures is considered. Various initial end-gas temperature and hydrogen concentration in the binary fuels are considered. Homogeneous ignition of stochiometric ammonia/hydrogen/air mixtures is firstly calculated. It is found that $H_2$ addition significantly promotes autoignition, even if the amount of addition is small. For ammonia/air mixtures and ammonia/hydrogen/air mixtures with low hydrogen mole ratios, it is found from chemical explosive mode analysis results that $NH_2$ and $H_2NO$ are most important nitrogen-containing species, and R49 ($NH_2$ $+NO<=>N_2+H_2O$) is a crucial reaction during thermal runaway process. When the hydrogen mole ratio is high, the nitrogen-containing species and reactions on chemical explosive mode becomes less important. Moreover, a series of one-dimensional simulations are carried out. Three end-gas autoignition and combustion modes are observed, which includes forcibly ignited flame propagation, autoignition (no detonation), and developing detonation. These modes are identified within wide ranges of hydrogen contents and initial end-gas temperatures. Furthermore, chemical kinetics at the reaction front and autoignition initiation locations are also studied with chemical explosive mode analysis. Finally, different thermochemical conditions on knocking intensity and timing are investigated. It is found that a higher initial temperature or a higher $H_2$ content does not always lead to a higher knocking intensity, and the knocking timing decreases with the reactivity of end-gas.

© 2021 Hydrogen Energy Publications LLC. Published by Elsevier Ltd. All rights reserved.

## Introduction

To reduce $CO_2$ emissions from fossil fuel combustion, alternative fuels are in high demand. Ammonia ($NH_3$) is promising, since it is a carbon-free fuel and also a hydrogen ($H_2$) energy carrier (17.8% hydrogen by mass) [1–7]. Compared with hydrogen, $NH_3$ is easier to be liquefied and thus safer to be stored and transported. Besides, $NH_3$ is also a potential fuel for internal combustion (IC) engines due to its high octane rate [1]. However, compared with conventional hydrocarbon fuels, lower combustion intensity of $NH_3$ (resultant lower burning velocity, longer ignition delay time, and higher minimum ignition energy, etc.) makes wide use of ammonia for power still challenging [8,9].

To circumvent the foregoing disadvantages, more chemically reactive additives are often used to constitute blending fuels [10–15]. For instance, Dai et al. [11] studied the autoignition behaviour of $NH_3/H_2$ at high pressures. They find that ignition enhancing effect from $H_2$ addition is related to formation and decomposition of hydrogen peroxide ($H_2O_2$) species. Chen et al. [12] studied the effects of $H_2$ addition on high-temperature autoignition of $NH_3$. Their experimental results show that the ignition delay time decreases nonlinearly with $H_2$ addition. Wang et al. [16] investigated the combustion properties of $NH_3/H_2$ mixtures under spark ignition engine (SIEs) conditions. It is shown that a higher compression ratio is possible for $NH_3/H_2$ blends due to their knock resistance, compared to hydrocarbon fuels. However, they did not analyse knocking mechanism with $NH_3/H_2$ blends.

Knocking combustion has become a stumbling block for SIEs with high compression ratio [17–21]. It is caused by end-gas autoignition and associated with the interactions between acoustic wave and end-gas chemical reaction [22]. Furthermore, end-gas autoignition refers to the phenomena, in which autoignition of unburnt gas (end-gas) occurs before arrival of a forcibly ignited premixed flame under pressure wave disturbance in a confined chamber. Besides, the coherent coupling between the pressure wave and reactive front may induce detonation, leading to more severe super knock process. Therefore, knock propensity and suppression are outstanding issues for technological improvement and innovation of SIEs, such as utilization of new fuels (e.g., ammonia or hydrogen).

There have been intensive studies relevant to engine knocking in the literature. Detailed visualizations are made through high speed photograph by numerous experiments, especially in engine testbeds and rapid compression machines [23–25]. For instance, Zhou et al. [25] investigated end-gas autoignition and detonation development of gasoline fuel in a confined space. They identified three combustion modes, i.e., end-gas autoignition, end-gas autoignition without detonation, and end-gas autoignition with detonation development. Qi et al. [23] discussed the effects of thermodynamic states on end-gas combustion mode. They pointed out that detonation is more likely to happen with increasing initial pressure when the compression ratio is the same.

Moreover, high-fidelity simulations were also performed to study end-gas autoignition behaviours [26–36]. For instance, Terashima et al. [31–34] performed one-dimensional (1D) simulations to unveil the mechanisms of pressure wave development in end-gas autoignition during knocking combustion. They find that the amplitude of pressure oscillations is affected by low-temperature chemistry and strong pressure wave is induced by an exothermic spot. Yu et al. [35,36] studied end-gas autoignition and detonation development of stoichiometric hydrogen/air and iso-octane/air mixtures at different initial thermal states. They found that autoignition and detonation development are facilitated by increasing the reactivity of end-gas. Pan et al. [28] also performed 1D simulations of stoichiometric $H_2$/air mixture. They demonstrated that knocking intensity is affected by both initial autoignition events and the subsequent interactions between flame front and pressure wave. However, as far as we know, studies on end-gas autoignition and knocking combustion of $NH_3/H_2$ fuel blends under engine-relevant conditions are still limited.

In this work, detailed numerical simulations of end-gas autoignition and knocking combustion of $NH_3/H_2$ binary fuel blends will be conducted with detailed chemical mechanism. The homogeneous autoignition process will be first studied, considering various hydrogen mole ratios and initial temperatures. Then, through one-dimensional simulations of a reactor filled with $NH_3/H_2$/air mixture, end-gas autoignition and knocking combustion characteristics under engine-relevant conditions will be discussed. We will focus on the following aspects: (1) autoignition of $NH_3/H_2$ fuel blends; (2) effects of end-gas temperature and $H_2$ content in the binary fuels on knocking intensity and timing; and (3) key chemical features (i.e., the dominant thermophysical variable and reaction pathway) during autoignition of $NH_3/H_2$ end-gas.

## Physical model, numerical and analysis methods

### Physical problem

Autoignition and detonation development of ammonia/hydrogen/air end-gas in one-dimensional constant-volume reactor is studied in this work, and the physical model is illustrated in Fig. 1. This model is used to mimic a combustion chamber when a SI engine piston lies at the top dead centre, and has been successfully adopted in previous studies on knocking combustion [31–37]. Only half the reactor is considered, and the computational domain length is $L = 4$ cm. The initial pressure in the reactor is $P_0 = 5$ atm, which is close to the actual pressure of IC engine at the top dead centre [28]. No initial flows are present, i.e., $u_0 = 0$ m/s.

Premixed $NH_3/H_2$/air mixture is uniformly distributed in the reactor (i.e., the initial compositions are the same in the reactor). Different compositions are considered, parameterized by $H_2$ mole ratio in the $NH_3/H_2$ binary blend fuels. Specifically, the $H_2$ mole ratio is defined as $a_{H_2} = X_{H_2}/(X_{H_2} + X_{NH_3})$, where $X$ is mole fraction, and $0 \leq a_{H_2} \leq 1.0$ is studied in our analysis. Besides, the mixture equivalence ratio $\varphi$ is defined following Refs. [14,38], assuming that the products of complete $NH_3$ oxidation are $N_2$ and $H_2O$, i.e., $2NH_3 + 1.5O_2 \rightarrow N_2 + 3H_2O$. In this study, the equivalence ratio is $\varphi = 1.0$, unless otherwise stated. It is also assumed that $H_2$ and $NH_3$ share the same equivalence ratio. Therefore, the
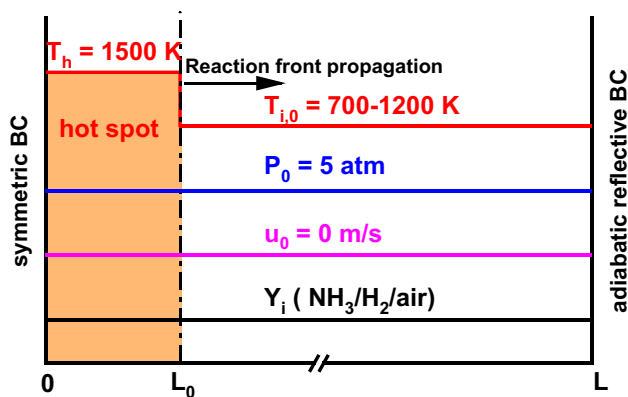
**Fig. 1** – **One-dimensional reactor with NH₃/H₂/air mixture.**

initial compositions of $NH_3$, $H_2$, $O_2$ and $N_2$ species in the end-gas follow

$$\varphi\left[(1-a_{H_2})X_{NH_3}+a_{H_2}X_{H_2}\right]+(0.75-0.25a_{H_2})\left(X_{O_2}+3.76X_{N_2}\right). \quad (1)$$

As shown in Fig. 1, a propagating flame is forcibly ignited by a flat ignition kernel of size $L_0 = 2$ mm with temperature of $T_h = 1500$ K near the left boundary. It should be noted that either changing the hot spot size or temperature will affect the strength of pressure wave triggered by the hot spot [28,33]. In our study, we also discuss the their effects and the results can be Supplemental Material. For the end-gas outside the hot spot, the initial temperature $T_{i,0}$ is spatially uniform. We consider $T_{i,0} = 700-1200$ K, relevant to the end-gas temperatures in IC engines [22]. After the flame is successfully ignited, the $NH_3/H_2/air$ end-gas is continuously compressed by the right-propagating flame front. A secondary, but more reactive, autoigniting hot spots may occur therein due to the pulsed pressure wave from the thermal runaway of the ignition kernel, which further leads to strong pressure wave [32,37]. Shuttling of these pressure waves in the reactor may result in knocking combustion subject to the local gas dynamics [35]. Furthermore, the turbulence effects on end-gas autoignition are not included, which is deemed reasonable since when a hot spot evolves initially, the flows would be generally laminar [39]. Moreover, the turbulence timescales can be around three orders of magnitudes larger the autoignition ones under IC engine-relevant conditions [40].

### Numerical method

One-dimensional governing equations of momentum, energy, and species mass fractions for compressible multi-species reacting flows in the foregoing physical problems are solved with a well-validated code A-SURF (Adaptive Simulation of Unsteady Reactive Flow) [41,42]. The accuracies of this solver have been confirmed in many previous work, including flame propagation [43,44], detonation development [45–47], and end-gas autoignition [35–37].

The governing equations are discretized with the cell-centred finite volume method. An operator splitting approach of second-order accuracy is used to decouple the chemical reaction and flow calculations. In the first fractional step, the non-reactive flows are solved. Second-order

Runge–Kutta, MUSCL – Hancock, and central differencing schemes are used to discretize the unsteady, convection and diffusion terms, respectively. In the second fractional step, the reaction term is integrated using a point implicit method. More details about the numerical implementations can be found in Refs. [41,42].

Dynamically adaptive mesh refinement algorithm [48] is adopted to accurately capture the reaction front and shock/pressure wave with a reduced computational cost. The maximum level of refinement is 8, corresponding to the finest cell size of about 3.9 μm. It is found that the reaction front evolutions and time history of knocking are not affected by further mesh refinement. The minimum time step is $5 \times 10^{-11}$ s, which guarantees that the CFL (Courant–Friedrichs–Lewy) number is less than 0.4. As marked in Fig. 1, symmetric condition is enforced for the left boundary ($x = 0$), whilst adiabatic reflective wall condition for the right one ($x = L$). The wall condition effects have been discussed by Terashima et al. [31,32] and Liberman et al. [49], and it is concluded that chamber wall condition may affect near-wall hot spot development and/or autoignition locations under some end-gas temperature conditions. Moreover, a detailed chemical mechanism (34 species and 204 elementary reactions) [50] is used, which has been validated against the experimental data and good accuracies are confirmed in predicting ignition delay time and laminar flame speed alike [51].

### Computational diagnostics approach

The chemical explosive mode analysis (CEMA) [52,53] is used to the identify the unsteady chemical information in end-gas autoignition. It is an advanced computational diagnostics approach to detect critical combustion features (e.g. ignition, extinction, detonation development) and pinpoint the controlling mechanisms through eigen analysis of chemical Jacobian matrix [54–58]. Complete descriptions about CEMA can be found in Refs. [52,54–56], and here only brief information is presented for sake of completeness. For a typical chemical reaction system, the governing equations of species and temperature read

$$\frac{D\varphi}{Dt}=\omega(\varphi)+s(\varphi), \quad (2)$$

where $D(\cdot)/Dt$ is the material derivative. $\varphi$ is the vector of local species mass concentrations $C_i$ and temperature $T$, i.e., $\varphi = [C_1, \cdots C_n, T]$. In the RHS (right hand side) of Eq. (2), $\omega(\varphi)$ is the vector of the chemical source terms, whilst $s(\varphi)$ denotes the non-chemical terms (e.g., diffusion). The CEMA is based on eigen analysis of the Jacobian matrix $J_\omega$ of the chemical source term $\omega(\varphi)$. A chemical mode is defined as an eigenmode of $J_\omega$, which contains an eigenvalue and the corresponding eigenvectors. Accordingly, a chemical explosive mode (CEM) is the chemical mode whose real part of the eigenvalue $\lambda_e$ is positive, i.e., $\text{Re}(\lambda_e) > 0$. This indicates the propensity of chemical explosion when the mixture is isolated [52].

The contribution of a chemical species or temperature towards a CEM can be quantified by explosion index (EI) [52].

$$\text{EI}=\frac{\text{diag}|a_e b_e|}{\text{sum}(\text{diag}|a_e b_e|)}, \quad (3)$$

where $a_e$ and $b_e$ are respectively the right and left eigenvectors, and "diag| • |" denotes the elementwise absolute values. The elements of **EI** range from 0 to 1. Higher **EI** value indicates higher contribution of the species or temperature in a CEM. Besides, the contribution of a reaction to a CEM is measured by participation index (PI) [52].

$$PI = \frac{|(b_e \cdot S) \otimes R|}{sum(|(b_e \cdot S) \otimes R|)}, \tag{4}$$

where **S** is the stoichiometric coefficient matrix and **R** is the vector of net reaction rate. "$\otimes$" represents the element-wise multiplication of two vectors. All the elements of **PI** lie within [0, 1], and the reaction is dominant in the CEM if its PI is close to unity.

---

## Results and discussion

### Homogeneous ignition

Fig. 2 shows the ignition delay time of stochiometric $NH_3/H_2/$ air mixtures as a function of $H_2$ mole ratio $a_{H_2}$ under different initial temperatures $T_0$ in a zero-dimensional constant-volume reactor. The ignition delay time $\tau_i$ is defined as the instant when the heat release rate reaches its peak. One can see that $\tau_i$ becomes shorter when the initial end-gas temperature $T_0$ is increased, regardless of $a_{H_2}$. Besides, for a constant initial temperature (such as 1000 K), $\tau_i$ monotonically decreases with $H_2$ mole ratio $a_{H_2}$. For instance, when $a_{H_2} = 0$, it is about 1400 m s. However, $H_2$ addition significantly promotes autoignition, even if the amount of addition is small (e.g., $a_{H_2} = 0.1$, the corresponding ignition delay for $T_0 = 1000$ K is reduced to about 26 m s). This tendency is also observed in Refs. [12,59]. Beyond a critical value of $a_{H_2}$ (about 0.15), the dependence of $\tau_i$ on hydrogen mole ratios $a_{H_2}$ is gradually reduced. Note that the slopes of $\tau_i$ of the initial temperatures under 1100 K become almost flattened when $a_{H_2}$ is beyond a certain level. This indicates that the reactivity of binary fuel
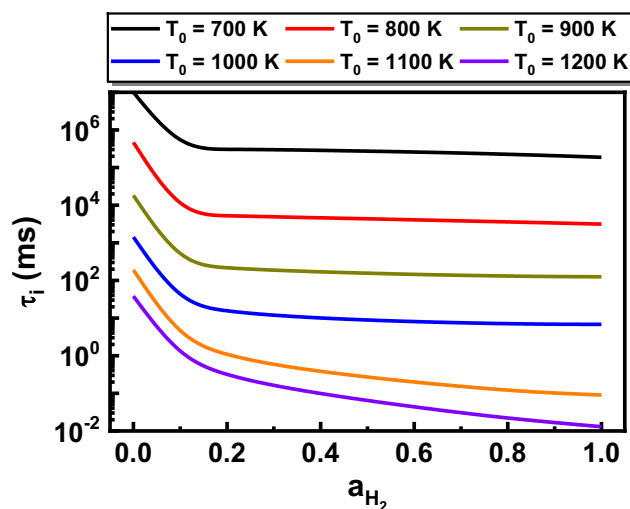
blends cannot be further significantly enhanced by increasing $H_2$ content under these temperatures.

To further understand homogeneous ignition of stochiometric $NH_3/H_2/$air mixtures, Fig. 3 shows the time evolutions of the real part of the eigen value of chemical Jacobian matrix, $Re(\lambda_e)$, EIs of the dominant species, and PIs of dominant elementary reactions. The $H_2$ mole ratio is $a_{H_2} = 0.1$, whereas the initial temperature is $T_0 = 1000$ K. Note that only the thermochemical variables and reactions with the highest EI and PI values are plotted. It is seen from Fig. 3(a) that zero-crossing of $Re(\lambda_e)$ is observed when the autoignition occurs at about 26 m s, corresponding to fast transition from unburned to burned states [52].

There are two induction stages, respectively corresponding to chemical runaway (chain-branching) and thermal runaway (thermal ignition) processes, as denoted in Fig. 3(b). Chemical (thermal) runaway is identified by the dominance of species (or temperature) explosion indices, i.e., $EI(Y_i)$ ($EI(T)$) is higher than $EI(T)$ ($EI(Y_i)$). See Fig. 3(b), from beginning to the moment denoted by the black circle, $EI(Y_i)$ is always higher than $EI(T)$, thus this period is considered as the chemical runaway process. From the instant denoted by the black circle to the end, $EI(T)$ is always higher than $EI(Y_i)$, thus this period is considered as a thermal runaway process. Their durations, $\tau_{chem}$ and $\tau_{therm}$, are 15.9 m s and 10.2 m s, respectively. The ratio



Fig. 2 − Ignition delay time of stochiometric $NH_3/H_2/$air mixtures with different $H_2$ mole ratios and initial temperatures. The initial pressure is 5 atm.
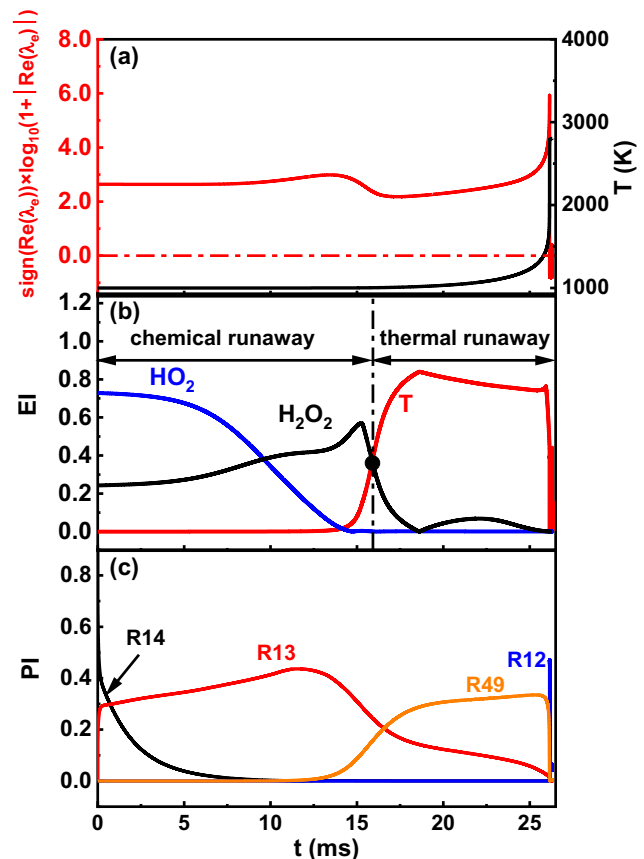


Fig. 3 − Time evolutions of (a) real part of eigenvalue $Re(\lambda_e)$, heat release rate, (b) EIs, and (c) PIs of dominant elementary reactions. $a_{H_2} = 0.1$ and $T_0 = 1000$ K. Black circle in (b): onset of thermal runaway process.

between the duration of thermal runaway process and overall ignition delay ($\tau_i = \tau_{chem} + \tau_{therm}$), $\theta_r = \tau_{therm}/\tau_i$, is quantified, and in this case $\theta_r \approx 0.39$. The lasting thermal runaway process is an important feature of $NH_3$ autoignition and renders it a Semenov-type autoignition, which is not observed in other hydrocarbon fuels [38]. For hydrocarbon fuels, $\tau_{therm}$ is typically much smaller than $\tau_{chem}$, which indicates that, after the radical pools are established, the time it takes for the reactive system to reach the thermal explosion condition is much shorter [60].

In the chemical runaway process (before 15.9 m s), two elementary reactions are dominant, R14 and R13, as found in Fig. 3(c). They correspond to formation and/or consumption of $HO_2$ radical, see Table 1. However, after 15.9 m s, in the thermal runaway process, R49 (exothermic reaction) is important for a majority period of thermal runaway process, through which $NH_2$ and NO react to produce the combustion products, i.e., $N_2$ and $H_2O$. Note that the activation energy of R49 is zero, and therefore exponential temperature dependence is not present for this elementary reaction. This leads to a less temperature-sensitive and hence relatively slow thermal runaway process in Fig. 3. Accumulation of $H_2O$ species ultimately promotes the reaction of H and OH through R12 at the end of the autoignition with strong heat release.

The controlling state variables and elementary reactions of stochiometric $NH_3/H_2/air$ mixtures with a range of $H_2$ mole ratios ($a_{H_2} = 0 - 0.9$) and initial temperatures ($T_0 = 800 - 1600$ K) are calculated and summarized in Table 2. The controlling state variables and reactions are respectively identified from the highest EI and PI values (the criteria is same with that used in Fig. 3). For $NH_3/air$ mixtures ($a_{H_2} = 0$), the reaction systems start with the chain initiating reactions, R28 or R38 (see Table 1), in which the fuel ammonia dehydrogenation proceeds with a third body or $O_2$ to generate radicals, including $NH_2$, H, and $HO_2$. $NH_2$ further reacts with $O_2$ through R43 to provide $H_2NO$ and O, whilst $H_2NO$ radical is consumed through R101. The foregoing reaction pathway of ammonia/air mixture is also observed for close initial parameter conditions with computational singular perturbation method [38].

For $NH_3/H_2/air$ mixtures with low hydrogen mole ratios, i.e., $a_{H_2} = 0.1$ and 0.5, if $T_0 < 1200$ K, the contributions of controlling state variables and elementary reactions towards

CEM are generally similar to those in Fig. 3. However, when the temperature is increased to 1200 K and above, $NH_2$ or H shows the largest influence on the CEM. Note that with low hydrogen blending, R49 becomes the sole nitrogen-containing dominant reaction with significant contribution towards the CEM. When the hydrogen mole ratio is high (e.g., $a_{H_2} = 0.9$), the nitrogen-containing species and reactions on CEM becomes less important, and the homogeneous ignition process is mainly controlled by R1, R4, R12 − 14 and R24.

Fig. 4 further quantifies the dependence of the thermal runaway time ratio $\theta_r$ on hydrogen mole ratio and initial temperature. For $NH_3/air$ mixtures ($a_{H_2} = 0$), $\theta_r$ decreases with higher initial temperature approximately linearly. For $NH_3/H_2/air$ mixtures, $T_0 = 1200$ K is loosely a critical temperature, as shown in Fig. 4. Specifically, when $a_{H_2} = 0.9$, $\theta_r$ decreases with higher initial temperature when $T_0 < 1200$ K, but it remains almost constant when $T_0 > 1200$ K. Considering the monotonic decrease of ignition delay with initial temperature from Fig. 2, $\tau_{therm}$ thereby decreases pronouncedly as $T_0$ increases $a_{H_2} = 0.9$. However, the cases for $a_{H_2} = 0.1$ and 0.5 are more complicated. Specifically, $\theta_r$ first increases with $T_0$ before 1200 K, and then decreases. With the $\tau_i - T_0$ relations in Fig. 2, before $T_0 < 1200$ K, $\tau_{therm}$ generally decreases with $T_0$. This is because the $NH_2$ becomes more important when increasing initial temperature for $NH_3/H_2/air$ mixtures with low hydrogen mole ratios (as shown in Table 2).

### End-gas combustion mode

A series of one-dimensional detailed simulations with the configuration in Fig. 1 have been run with different hydrogen/ammonia ratios and end-gas initial temperatures. Different end-gas combustion modes are observed, which includes forcibly ignited flame propagation, supersonic autoignitive deflagration, and developing detonation. In this section, eight cases, A − H, are selected to elucidate the interactions between gas dynamics and chemical reactions behind these modes, and their parameters are summarized in Table 3. Note that for cases A − D the hydrogen mole ratio is 0.9 (low $NH_3$ percentage), whilst it is 0.1 (high $NH_3$ percentage) for cases E − H. Similar mode categories are also made in previous knocking studies with other fuels [31,35,37]. In the following, these combustion modes in the current binary fuel end-gas will be briefly presented, and the peculiar phenomena due to ammonia addition will be highlighted wherever necessary.

### Forcibly ignited flame propagation (cases A and E)
Fig. 5 shows the $x - t$ diagrams of temperature and pressure in cases A and E. The evolutions of their flame propagation speeds are shown in Fig. 6. In case A, it is seen from Fig. 5(a) that the flame front (FF) moves back-and-forth (resulting in a wavy trajectory) before 1.0 m s (corresponding to about 3.0 cm). This unsteady phenomenon of flame-shock interaction is also observed in closed reactors [61−64] and numerically studied by Pan et al. [28]. This is manifested by oscillating propagating speed (see Fig. 6(a)) and is caused by the interactions between the flame front and reciprocating pressure wave generated by the initial spark, as can be found from $x - t$ diagram of pressure of Fig. 5(a). After 1.0 m s, the reactor pressure is gradually elevated, albeit approximately spatially

| Table 1 − Dominant elementary reactions. | |
|---|---|
| Index | Reaction |
| R1 | $H + O_2 <=> O + OH$ |
| R4 | $OH + H_2 <=> H + H_2O$ |
| R12 | $H_2O + H_2O <=> H + OH + H_2O$ |
| R13 | $H + O_2 + M <=> HO_2 + M$ |
| R14 | $HO_2 + H <=> H_2 + O_2$ |
| R22 | $H_2O_2 + M <=> OH + OH + M$ |
| R24 | $H_2O_2 + H <=> HO_2 + H_2$ |
| R28 | $NH_3 + M <=> NH_2 + H + M$ |
| R31 | $NH_3 + OH <=> NH_2 + H_2O$ |
| R38 | $NH_2 + HO_2 <=> NH_3 + O_2$ |
| R43 | $NH_2 + O_2 <=> H_2NO + O$ |
| R49 | $NH_2 + NO <=> N_2 + H_2O$ |
| R77 | $NNH + O_2 <=> N_2 + HO_2$ |
| R101 | $H_2NO + O_2 <=> HNO + HO_2$ |

**Table 2 – Chemical information in homogeneous ignition of NH$_3$/H$_2$/air mixtures$^a$.**

| $a_{H_2}, T_0$ | Controlling thermochemical variables | Controlling reactions in chemical runaway stage | Controlling reactions in thermal runaway stage |
|---|---|---|---|
| 0.0, 800 K | NH$_2$, H$_2$NO, T | **R38, R101, R49** | **R49**, R12 |
| 0.0, 1000 K | NH$_2$, H$_2$NO, T | **R38, R43, R101** | **R49**, R12 |
| 0.0, 1200 K | NH$_2$, H$_2$NO, T | **R28, R43, R101, R49** | **R49**, R12 |
| 0.0, 1400 K | NH$_2$, H$_2$NO, T | **R28, R43, R49** | **R49**, R12 |
| 0.0, 1600 K | NH$_2$, N$_2$H$_2$, H$_2$, T | **R28, R43, R31, R49** | **R49**, R12 |
| 0.1, 800 K | HO$_2$, H$_2$O$_2$, NO$_2$, T | R14, R22, R13 | **R49**, R12 |
| 0.1, 1000 K | HO$_2$, H$_2$O$_2$, T | R14, R13 | **R49**, R12 |
| 0.1, 1200 K | NH$_2$, T | R14, R1, R13 | R13, **R49**, R12 |
| 0.1, 1400 K | NH$_2$, T | R14, R1, **R31** | **R31**, **R49**, R12 |
| 0.1, 1600 K | NH$_2$, T | R14, R1, **R31** | **R31**, **R49**, R12 |
| 0.5, 800 K | HO$_2$, H$_2$O$_2$, T | R14, R24, R13 | R13, **R49**, R12 |
| 0.5, 1000 K | HO$_2$, H$_2$O$_2$, NO, T | R14, R13 | R13, **R49**, R12 |
| 0.5, 1200 K | NH$_2$, T | R14, R1, R13 | R13, **R49**, R12 |
| 0.5, 1400 K | NH$_2$, T | R14, R1 | R1, **R49**, R12 |
| 0.5, 1600 K | NH$_2$, T | R14, R1 | R1, R4, R12 |
| 0.9, 800 K | HO$_2$, H$_2$O$_2$, T | R14, R24, R13 | R13, R12 |
| 0.9, 1000 K | HO$_2$, H$_2$O$_2$, T | R14, R13 | R13, R4, R12 |
| 0.9, 1200 K | H, T | R14, R1, R13, R4 | R4, R12 |
| 0.9, 1400 K | H, T | R14, R1, R4 | R4 |
| 0.9, 1600 K | H, T | R14, R1, R4 | R4 |

$^a$ The bold indices indicate the nitrogen-containing elementary reactions.

uniform, due to adiabatic compression by the moving flame front. The NH$_3$/H$_2$/air end-gas is gradually consumed by the steadily encroaching flame at a speed of 15.6 m/s, slightly higher than the laminar flame speed predicted with initial gas compositions, as seen from Fig. 6(a). No localized autoignitive spots or thermal explosion occur in the end-gas. Until being completely burnt, the end-gas is still experiencing the first stage of the induction period, i.e., chemical runaway process, which is evidence by the time evolutions of EIs at right boundary. This is deemed a knocking-free combustion process since no pressure peak is found near the reactor wall.

Fig. 5(b) shows the counterpart results of case E (the same end-gas temperature $T_0$, but higher ammonia content, compared to case A). Like case A, only the forcibly ignited

flame propagates, without end-gas autoignition. However, it takes longer time to completely consume the fuel (around 22 m s), due to the slower flame propagating speed (about 1.4 m/s) than that in case A (15.6 m/s), which are marked in Fig. 6 for comparisons. This is reasonable because more ammonia addition in case E leads to slower chemical reactions. Besides, since the weaker pressure wave (the pressure wave intensity is 1.1, lower than that of 1.56 in case A) emanated from the ignition hot spot, less pronounced flame front oscillations are observed, which quickly decays after 1.6 m s (about 0.7 cm, see Fig. 6) due to energy dissipation and wave interactions in the closed reactor. Thereby, after that, the flame actually propagates in a relatively quiescent environment, and the propagation speed is very closed to the
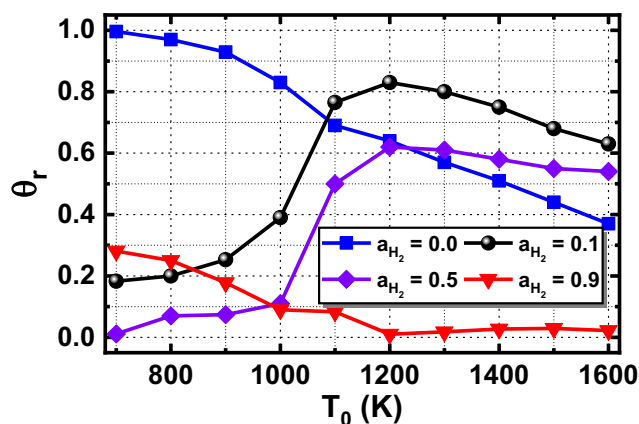


**Fig. 4 – Thermal runaway time ratio of stochiometric NH$_3$/H$_2$/air mixtures with different H$_2$ mole ratios and initial temperatures.**

**Table 3 – Combustion mode in ammonia/hydrogen/air end-gas.**

| Case | $a_{H_2}$ (−) | $T_0$ (K) | Combustion mode | Knocking |
|---|---|---|---|---|
| A | 0.9 | 800 | forcibly ignited flame propagation | No |
| B | 0.9 | 900 | developing detonation | Yes |
| C | 0.9 | 1000 | developing detonation | Yes |
| D | 0.9 | 1100 | developing detonation | Yes |
| E | 0.1 | 800 | forcibly ignited flame propagation | No |
| F | 0.1 | 900 | supersonic autoignitive deflagration | Yes |
| G | 0.1 | 1000 | supersonic autoignitive deflagration | Yes |
| H | 0.1 | 1100 | supersonic autoignitive deflagration | Yes |
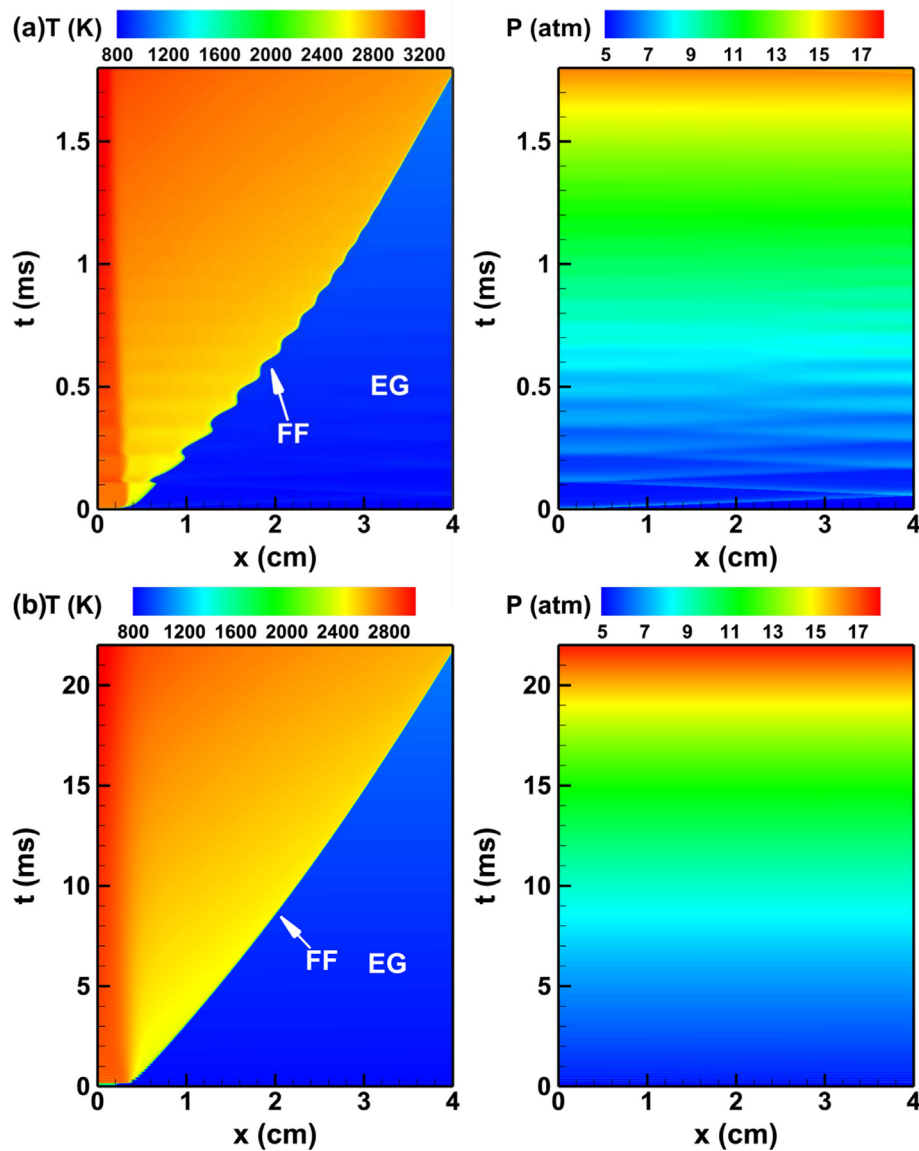
Fig. 5 $-$ $x-t$ diagrams of temperature and pressure in case (a) A and (b) E. FF: flame front, EG: end-gas.

laminar flame speed (about 0.74 m/s) predicted with the initial end-gas thermochemical composition.

*Supersonic autoignitive deflagration (cases F, G and H)*
In cases F, G and H with low hydrogen mole ratio ($a_{H_2} = 0.1$), it is observed from our simulation that knocking is caused by end-gas autoignition. The latter occurs when the flames propagate towards the reactor wall; however, no detonations develop before the end-gas is fully burnt. As tabulated in Table 3, these three cases have various initial temperatures ($T_0 = 900$, 1000 and 1100 K, respectively). In this sub-section, their respective autoignition processes will be discussed in Fig. 7, and their propagation speeds are plotted in Fig. 8.

Fig. 7(a) illustrates the $x-t$ diagrams of temperature and pressure in case F. The reader should be reminded that here only the information within limited space and time is presented, focusing on the localized unsteady autoignition event. The pressure wave from the ignited flames decays at around

2.8 m s (see the speed profiles from Fig. 8(a)) and therefore the end-gas is not aerodynamically perturbed afterwards. With continuous compression caused by the right-propagating flame front, the autoignition starts at about 13.44 m s (i.e., AF in Fig. 7(a)). Starting at $x = 3.7$ cm, the autoignition front AF continuously propagates rightward supersonically with a peak speed of about 1742 m/s (see Fig. 8(a)) and knocks on the wall at about 13.45 m s. Before the autoignition event begins, the end-gas is experiencing the thermal runaway stage.

Fig. 7(b) and (c) and show the $x-t$ diagrams of temperature and pressure in cases G and H. Compared with case F, the reactivity of the end-gas in cases G and H is enhanced with higher initial temperatures (1000 K and 1100 K, respectively). It is seen from Fig. 7(b) and (c) and that the corresponding evolutions are similar to those of case F. Nonetheless, when end-gas autoignition occurs, the flame front FF locates at $x = 2.2$ cm in case G and $x = 1.1$ cm in case H, shorter than that of case F (i.e., 3.3 cm). These locations are determined not only by the
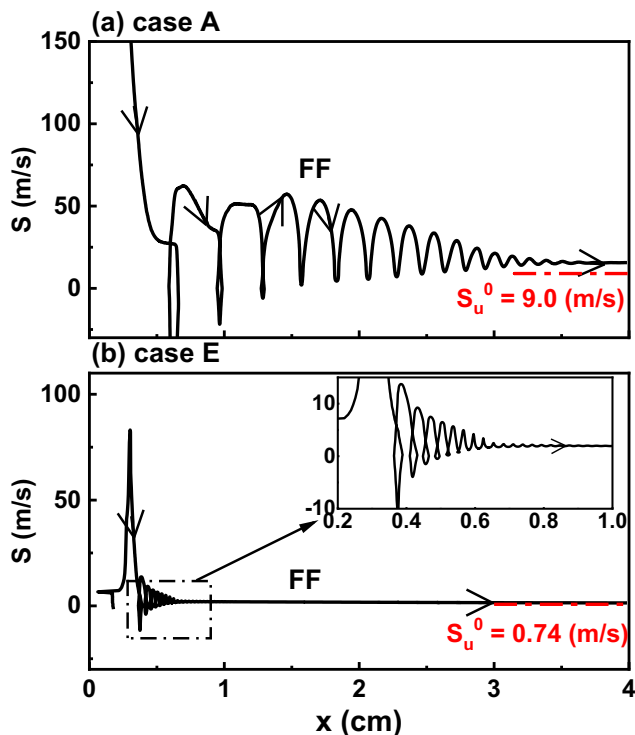
Fig. 6 — Reaction front propagation speed in cases (a) A and (b) E. $S_u^0$: laminar flame speed based on respective initial end-gas properties. See Fig. 5 for letter implications.

flame propagation speed, but also by the ignition delay of the end-gas. In cases F, G, and H, with increased end-gas initial temperature, the decrease of ignition delay is more significant than the increase of flame propagation speed. Thus, the corresponding autoignition location moves away from the reactor wall. As we can see from Fig. 8, the autoignition fronts AF propagate rightward supersonically in both cases, and the maximum speeds are up to about 8800 m/s in case G and 23,000 m/s in case H. This leads to the earlier knocking timing in cases G (6.42 m s) and H (2.226 m s). One can see from Figs. 7 and 8 that in these three cases with high ammonia mole ratio, autoignition always arises near the propagating flame front. How this mode varies in a range of initial end-gas temperature and hydrogen mole ratio will be further discussed in Section 3.2.4.

One can see that the induction period of the end-gas is under relatively quiescent environment since the pressure wave decays early. To clarify the evolutions of the spatial non-uniformity in the end-gas of cases F − H, Fig. 9 shows the time history of temperature differences between the end gas (select $x = 3.6$ cm as a representative location [33]) and reactor right wall (4.0 cm) from the above cases. It is seen that the temperature difference shows pronounced fluctuations before autoignition (i.e., 13.44 m s in case F, 6.40 m s in case G, and 2.25 m s in case H). The first maximum temperature difference is about 2.5 K in case F and about 2.7 K in cases G and H. This is induced by compression of the shuttling pressure waves inside the reactor. Note that the behaviours of temperature oscillation before autoignition in these cases are similar. This

is because the intensities of pressure wave generated by the hot spot in these cases are almost the same. The temperature difference when the pressure wave fully decays is 0.46 K in case F, 0.42 K in case G.

*Developing detonation (cases B, C and D)*
Fig. 10 shows the counterpart results of cases B − D, which have detonation development in the NH₃/H₂/air end-gas. These cases have the same hydrogen mole ratio, i.e., $a_{H_2} = 0.9$, but different initial temperatures (i.e., 900, 1000 and 1100 K). These are knocking cases caused by end-gas detonation development. Their propagating speeds are plotted in Fig. 11. In case B, before 1.0 m s, the flame front FF propagates and oscillates due to the pressure wave, which is not shown here. Seen from Fig. 10(a), end-gas autoignition occurs at about $x = 3.7$ cm, i.e., between the oscillating flame front FF (see the propagating speed variations in Fig. 11(a)) and reactor wall. The NH₃/H₂/air end-gas at $x > 3.6$ cm is consumed by the right-running supersonic autoignition front AF, with a peak speed of about 5356 m/s, as shown in Fig. 11. It is also seen from Fig. 10(a) that two pressure waves, respectively left- and right-propagating, are formed due to the foregoing auto-ignition event. In the residual end-gas near the wall, the pressure wave and AF couple with each other and hence detonative combustion proceeds (i.e., DF in Fig. 10(a)), resulting in the considerably high local pressure (over 40 atm) and heat release rate (about $10^{14}$ J/m³/s, results not shown here). However, this detonation wave cannot fully develop (see the propagation speed of DF in Fig. 11(a)), due to the insufficient space and complete consumption of the end-gas, as also seen from previous studies [31].

Fig. 10(b) shows the results from case C, which has higher end-gas temperature ($T_0 = 1000$ K) than that of case B. Before 0.4 m s, the flame front FF propagates and oscillates similar to case B. We can see from Fig. 10(b) that end-gas autoignition occurs near the reactor wall and at this instant the FF is located at $x = 2.2$ cm. This is caused by the continuous reactivity enhancement caused by the pressure wave reflection near the wall [35]. Subsequently, autoignition front propagates into the end-gas mixture at a speed of around 5000 m/s, as shown in Fig. 11(b). Moreover, because of the mutual enhancement between pressure wave and reaction front, a detonation wave DF is observed, travels towards the flame front at a speed of 1911 m/s, and finally collides with it at about $x = 2.3$ cm. It should be mentioned that the degree of pressure wave on the right wall is not high (the corresponding first pressure peak is 19.7 atm), due to the leftward propagation direction of the detonation wave.

As shown in Fig. 10(c), in case D, only normal flame propagation is observed at the beginning. The detonation is formed at about $x = 1.7$ cm due to the coherent coupling between local autoignition and pressure wave [35]. Subsequently, the detonative front DF propagates towards the reactor wall at a speed of around 2000 m/s (see Fig. 11(c)), which is slightly higher than the C − J speed of initial end-gas, 1914 m/s. The reactor wall suffers a strong knocking caused by the detonation (the corresponding maximum pressure is as high as 132 atm, as shown in Fig. 15(a)).
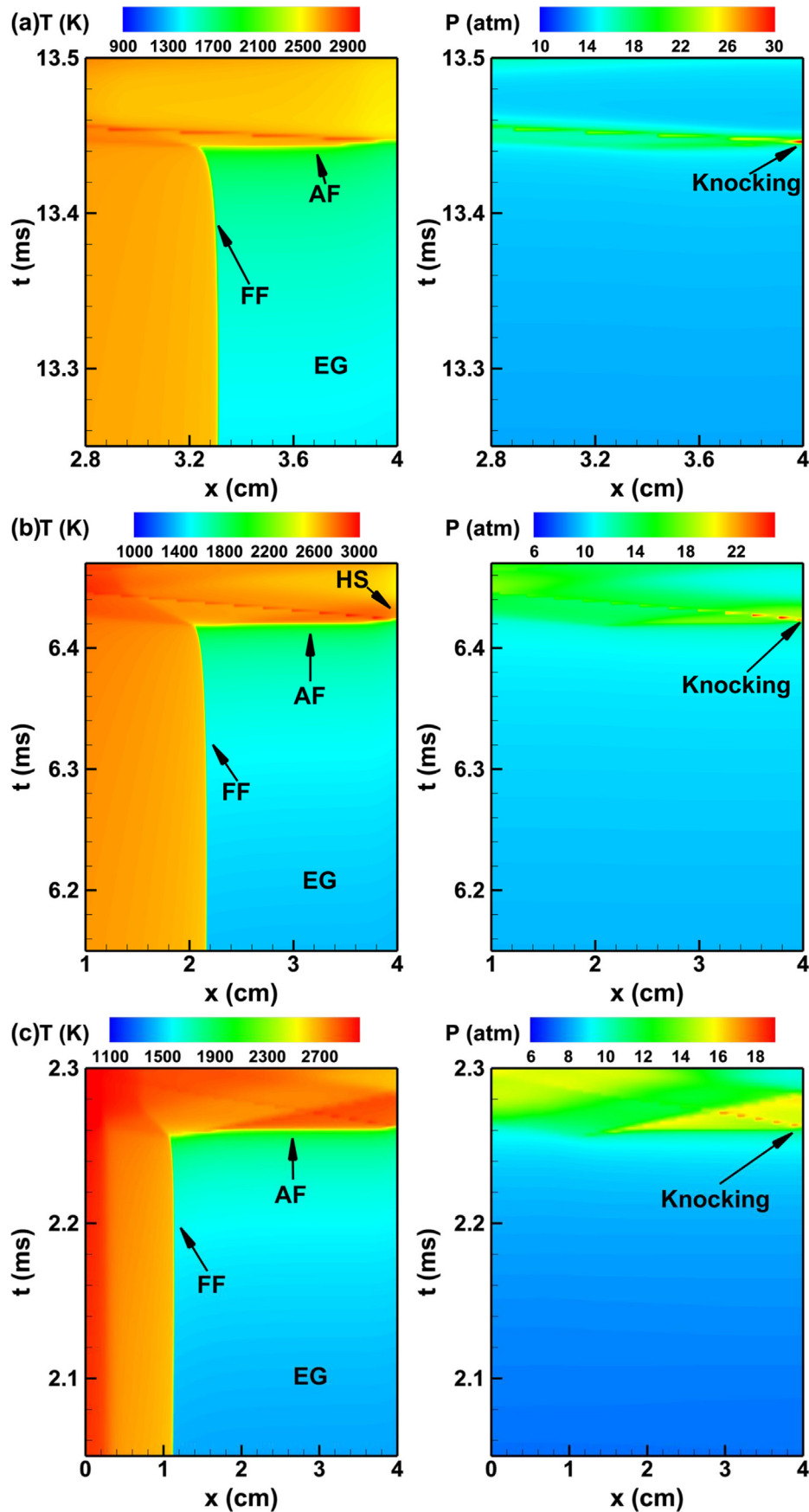
Fig. 7 — $x - t$ diagrams of temperature and pressure in case (a) F, (b) G, and (c) H. AF: autoignition front. See Fig. 5 for other letter implications.
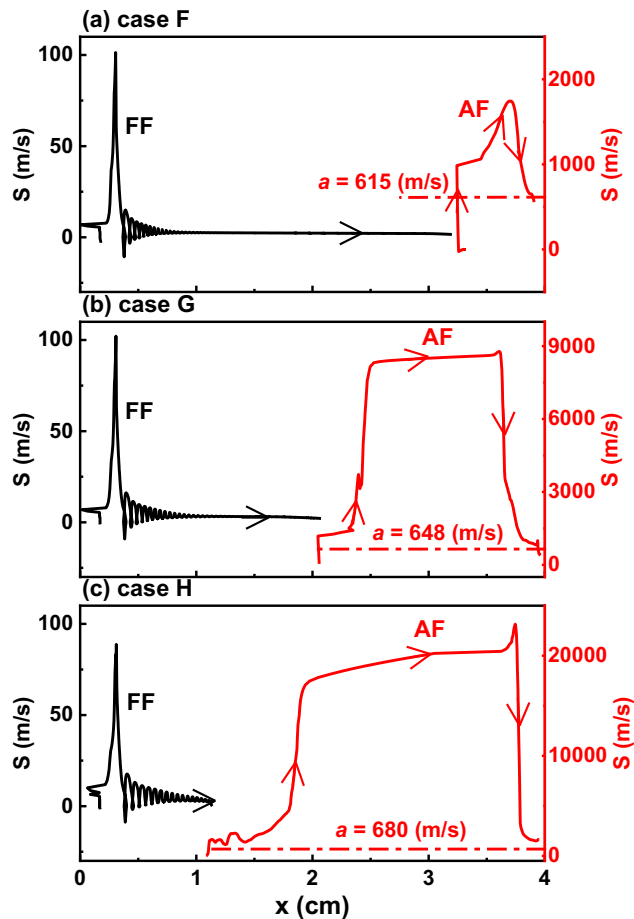
Fig. 8 – Reaction front propagation speed in cases (a) F, (b) G, and (c) H. *a* is the sound speed estimated from the respective initial end-gas properties. See Figs. 5 and 7 for letter implications.



Fig. 9 – Time history of temperature differences between end-gas ($x = 3.6$ cm) and reactor wall ($x = 4.0$): (a) F, (b) G, and (c) H.

*Summary of end-gas combustion mode*

Fig. 12 summarizes the end-gas combustion modes of stoichiometric $NH_3/H_2/air$ mixtures with various $H_2$ mole ratios ($a_{H_2} = 0.0 - 1.0$) and initial temperatures ($T_0 = 700 - 1200$ K). Except for the square symbols for normal flame propagation, the rest with end-gas supersonic autoigniting deflagration or detonation are coloured by the position of autoignition or detonation initiation.

For $NH_3/air$ mixture ($a_{H_2} = 0.0$), end-gas autoignition can happen when the temperature is above 1000 K, and their initiation location is at the wall. For $NH_3$ and $H_2$ binary blend fuels, normal flame propagation (including cases A and E presented above) proceeds for low initial temperature, e.g., below 900 K. This threshold temperature is close to that from $H_2/air$ end-gas knocking studies [28,37]. When $a_{H_2}$ is less than or equal to 0.2, if one further increase $T_0$, the $NH_3/H_2/air$ end-gas autoignition (such as cases F − H) is observable, but no detonation evolves. This is because the end-gas reactivity is enhanced by increasing temperature. As shown from the colouring of the circles in Fig. 12, autoignition can take place in the end-gas near or off the reactor wall surface. However, autoignition location changes nonmonotonically when the end-gas initial temperature is increased. This can be
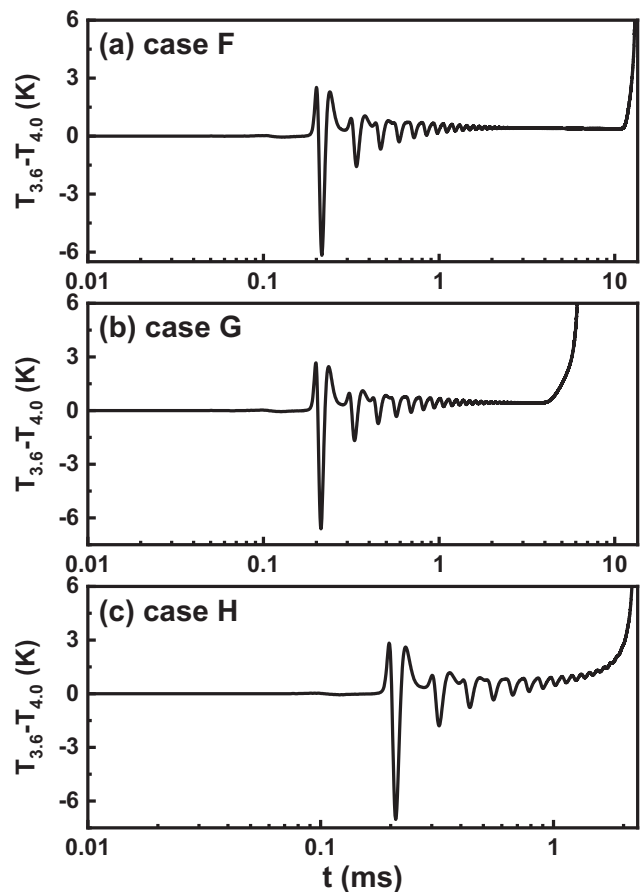
explained through the perspective of end-gas reactivity. It is noted that the end-gas at the autoignition location must have the shortest ignition delay, in other words, the highest reactivity, compared with the rest end-gas. For current study, the reactivity can be enhanced by both pressure wave disturbance and flame front compression. Thus, autoignition location can lie at the region either ahead of the flame front or within the pressure wave disturbance. Specifically, for $a_{H_2} = 0.1$, the pressure wave totally or approximately decays before autoignition. Therefore, autoignition always takes place ahead the flame front. The autoignition location is further associated with the flame front location and becomes smaller with higher end-gas initial temperature. For higher $a_{H_2}$, such as $a_{H_2} = 0.4$, the pressure wave shuttles before autoignition. This makes the problem more complicated. Different autoignition locations are observed. Autoignition takes place near the flame front when the temperature is 1100 K, while near the reactor wall surface when the temperature is 1200 K. That means the effect of pressure wave disturbance on the enhancement of reactivity is more significant for the latter case.

Furthermore, detonation in the end-gas can be initiated and develop (triangles in Fig. 12) when the hydrogen mole ratio in the binary fuels is sufficiently high. According to detonation propagation direction, two types of detonation
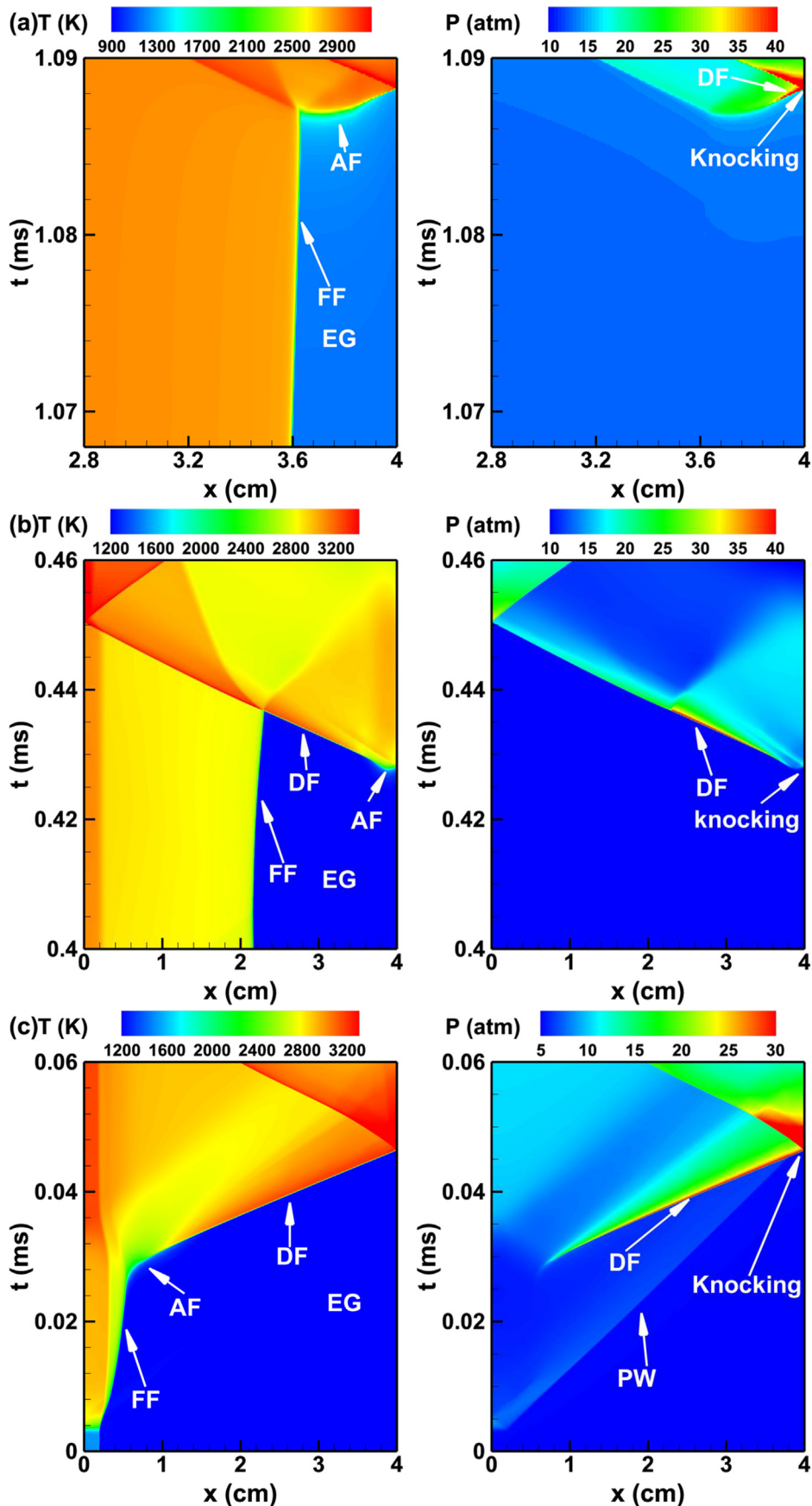
**Fig. 10 — $x - t$ diagrams of temperature and pressure in case (a) B, (b) C, and (c) D. DF: detonation front. See Figs. 5 and 7 for other letter implications.**
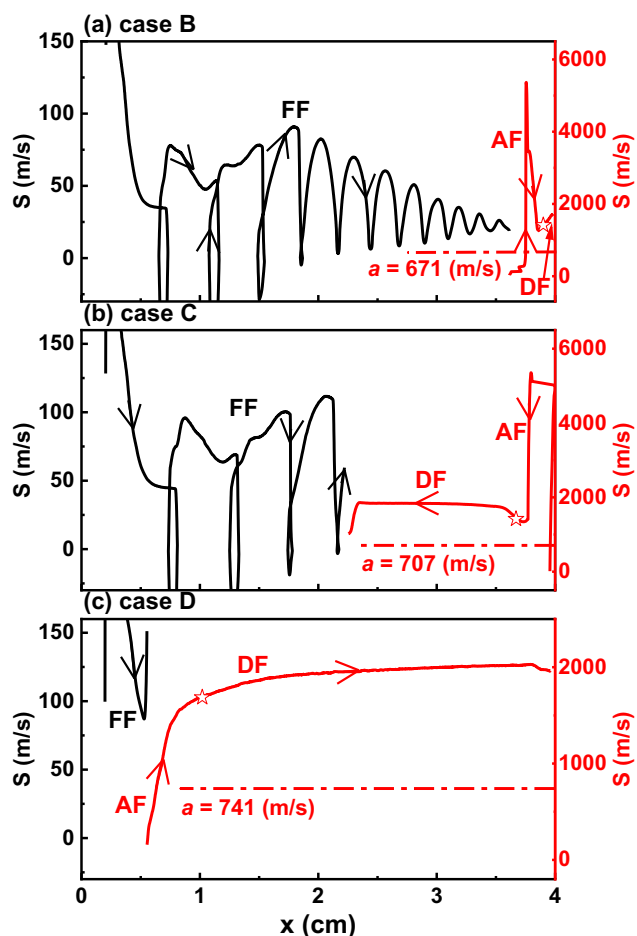
**Fig. 11** – Reaction front propagation speed in cases (a) B, (b) C, and (c) D. *a* is sound speed estimated from the respective initial end-gas properties. Empty pentagram: Detonation onset location. See **Figs. 5, 8 and 13** for letter implications.



**Fig. 12** – End-gas combustion mode under various hydrogen contents and initial temperatures. Square: normal flame propagation; circle: supersonic autoignitive deflagration; leftward triangle: left-running detonation; rightward triangle: right-running detonation.

development can be identified. The first one is right-propagating (e.g., cases B and D), whilst the second is left-propagating (e.g., case C). Moreover, when $a_{H_2} > 0.7$, detonation is always present when the end-gas temperature is above 800 K, due to the high reactivity from hydrogen addition.

*Evolutions of thermochemical state in end-gas combustion*

In this subsection, the CEMA will be used to further answer the following issues: (i) what are the key controlling mechanisms in the end-gas (i.e., FF, AF, and DF in Figs. 5, 7 and 10); and (ii) how the pressure wave and propagating flame front affect the controlling mechanisms in the end-gas near the reactor wall during end-gas autoignition.

*Thermochemical state inside the end-gas*
Fig. 13(a) and (b) and shows the spatial distributions of EIs and PIs across the flame front in cases A and E. The flame front is identified as zero-crossing of $Re(\lambda_e)$ [52], and marked as dash-dotted lines in Fig. 13(a) and (b) and . It is found that $H_2O$ is dominant very close to flame front (i.e., $x - x_F = 0$). However, attention should be paid to the chemically explosive end-gas, where $Re(\lambda_e)$ is positive, i.e., $x - x_F > 0$ in these two cases. Seen
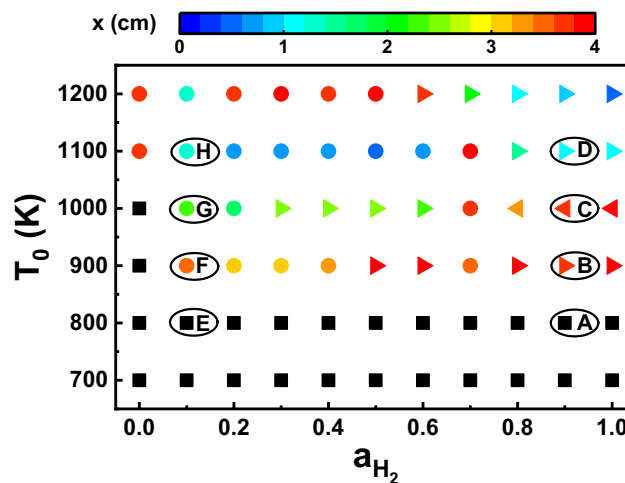
from Fig. 13(a), immediately ahead of the flame front, the contribution of temperature towards CEM is dominant, which indicates the slow thermal runaway process, as discussed in Section 3.1. At $x - x_F > 0.007$ cm, the contributions of $H_2O_2$ and $HO_2$ are dominant, indicating the local chain branching reactions. As seen from Fig. 13(a), R4 ($OH + H_2 \lessgtr H + H_2O$), R13 ($H + O_2 + M \Longleftrightarrow HO_2 + M$), and R77 ($NNH + O_2 \Longleftrightarrow N_2 + HO_2$) are found to be dominant towards CEM. The former two are related to formation and consumption of H radical, while the last corresponds to reaction of $HO_2$ radical. In case E from Fig. 13(b), same key species are identified. However, except for R13 and R77, the reaction R49 ($NH_2 + NO \Longleftrightarrow N_2 + H_2O$), instead of R4, is shown important near the flame front. This leads to slower flame propagating speed in Case E, as indicated in Fig. 6.

Fig. 13(c) and (d) and show spatial distributions of EIs and PIs in two knocking combustion cases, B and F. These two cases have the same initial temperature, but different $H_2$ content. $x_A$ is the autoignition front location, which is identified as zero-crossing of $Re(\lambda_e)$. In case B, it is seen from Fig. 13(c) that, HON is important around the autoignition front, whereas T has the largest contribution within the end-gas. This indicates that local autoignition is mostly undergoing the thermal runaway process, after a finitely long chemical runaway process. Only R4 is found to be important towards CEM within the explosive area. In case F from Fig. 13(d), similar evolutions of EIs are found. However, different PIs are observed, R1, R31 and R49 are shown to be important towards CEM, and the latter two respectively correspond to formation and consumption of $NH_2$ radical. In cases G and H, the local autoigniting end-gas is also experiencing the thermal runaway process with R1 being dominant towards CEM, as indicated from our simulation results.

Fig. 13(e) and (f) and show spatial distributions of EIs and PIs in two developing detonation cases, C and D. Here detonation front is identified as zero-crossing of $Re(\lambda_e)$. In case C,
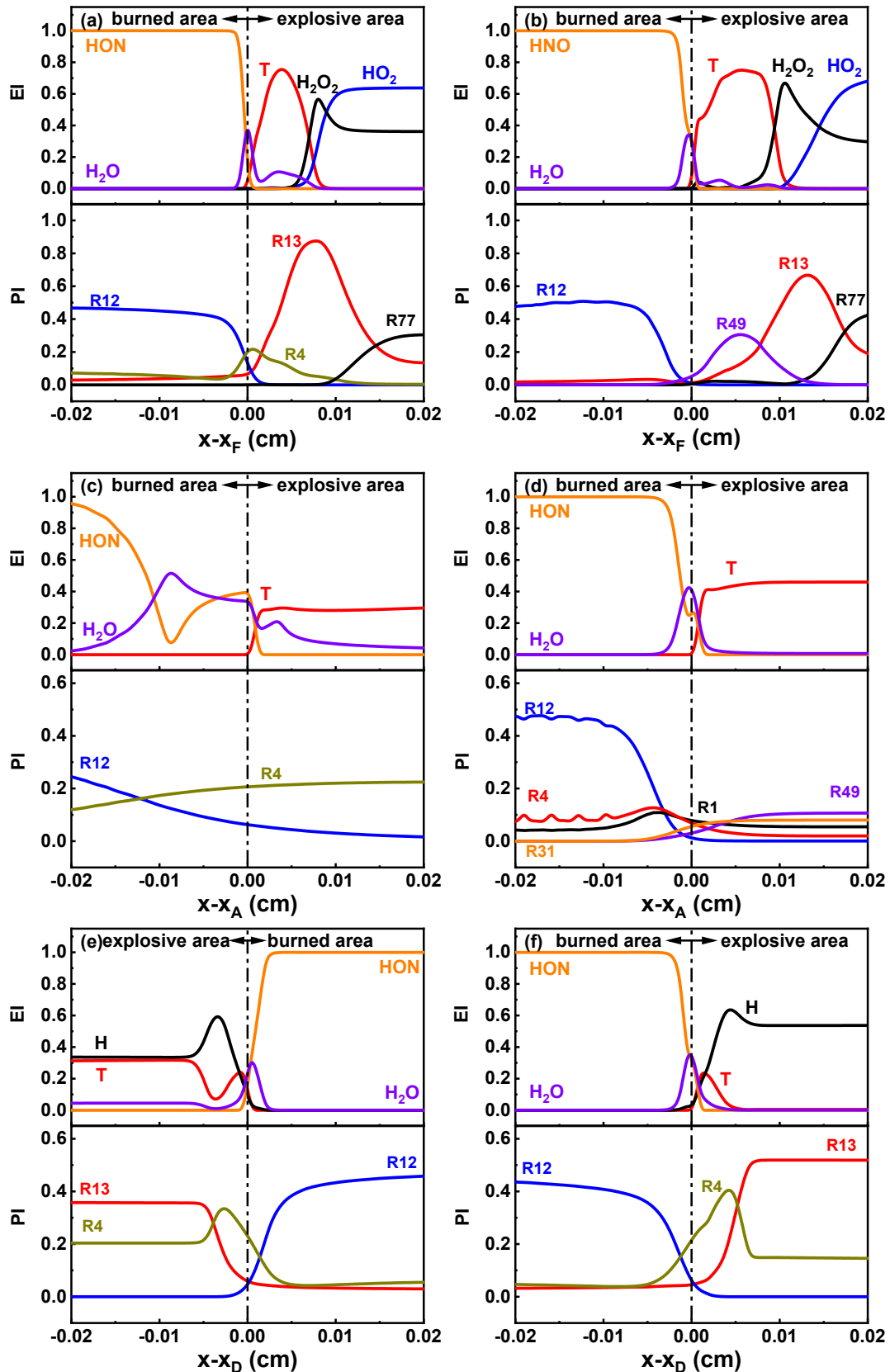
**Fig. 13** – Spatial distributions of species EIs and reaction PIs in (a) case A at t = 1.0 m s, $x_F$ = 2.75 cm, (b) case E at t = 15.0 m s, $x_F$ = 3.03 cm, (c) case B at t = 1.087 m s, $x_A$ = 3.80 cm, (d) case F at t = 13.44 m s, $x_A$ = 3.25 cm, (e) case C at t = 0.43 m s, $x_D$ = 3.00 cm, and (f) case D at t = 0.04 m s, $x_D$ = 2.72 cm $x_F$: flame position, $x_A$: autoignition front location, $x_D$: detonation front location.
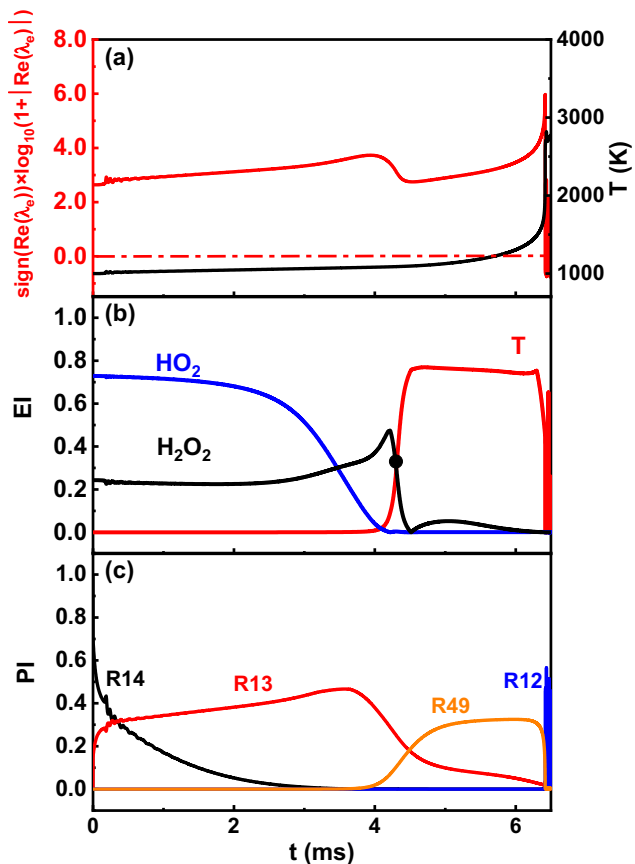
**Fig. 14 — Time evolutions of (a) real part of the eigenvalue, temperature, (b) EIs, and (c) PIs of dominant elementary reactions of case G at the position of autoignition initiation. Black circle in (b): onset of thermal runaway process.**

the contribution of H towards CEM is dominant within the explosive area, which indicates that the detonation front is mainly controlled by radical proliferation. Same with cases A and B, R4 and R13 are also found important towards CEM. See Fig. 13(f), similar distributions of EIs and PIs are found in case D, regardless of the different directions of propagation.

*Thermochemical state at autoignition initiation location*
The time dependent chemical information of end-gas at the autoignition initiation position is investigated here. Only

cases involving end-gas autoignition are considered, i.e., cases $B - D$, and $F - H$. The chemical information is extracted from a stable probe at the position of autoignition initiation of each case. As an example, Fig. 14 shows the results of case G. It should be noted that the initial end-gas thermochemical states of case G are just the same with those in Fig. 3. It is seen that the $Re(\lambda_e)$ keeps positive before end-gas autoignition occurs. Compared with the results in Fig. 3, the contributions of $HO_2$ and $H_2O_2$ are also dominant at the early stage, the difference is there are minor oscillations of the chemical time-scale which are related to the pressure wave disturbance. These minor oscillations can only be observed in chemical runaway stage. The temperature contribution becomes most important (see the circle in Fig. 14(b)) since t = 4.3 m s, indicating that the thermal runaway stage begins. Compared with homogeneous ignition, another difference is that the end-gas autoignition occurs much earlier. Besides, same with the results in Fig. 3(c), R14, R13, R49, and R12 are dominant. Note that R14 and R13 are respectively related to consumption and formation of $HO_2$ in the chemical runaway period. During the thermal runaway period, R49 and R12 become dominant, as discussed for the homogeneous ignition in Section 3.1.

The time dependent EIs and PIs at the position of auto-ignition initiation of rest cases are summarized in Table 4. It is noted that no nitrogen-containing species is found to be dominant through EIs in these cases except for case H. Specifically, $HO_2$ or $H_2O_2$ are found to be dominant in cases B, F and G, H is found to be dominant in cases C and D. Whilst in case H, nitrogen-containing species $NH_2$ is identified to be dominant. Besides, seen from PIs, R14, R13, and R12 are crucial reactions in all cases, and R49 is identified to be important for cases $F - H$. The PIs are similar with those shown in Table 1. Moreover, it is found that the proportion of thermal runaway

**Table 4 — Time dependent EIs and PIs identified with CEMA in cases $B - D$ and $F - H$.**

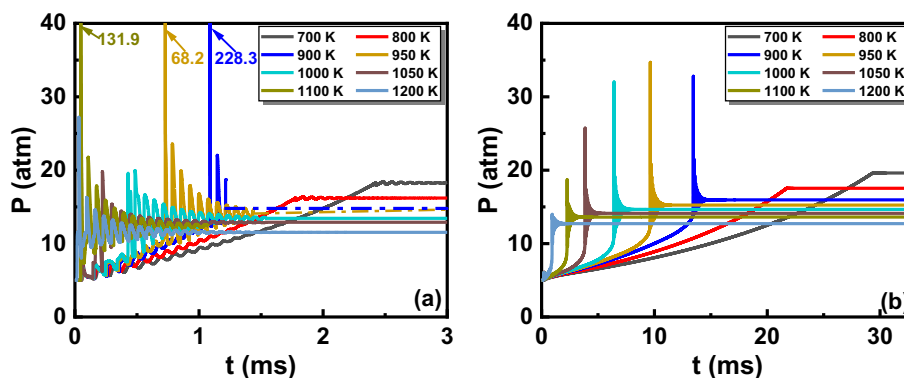| Case | EIs | PIs | $\theta_r$ |
|---|---|---|---|
| B | $HO_2$, $H_2O_2$, T | R14, R13, R12 | 0.023 |
| C | $HO_2$, H, T | R14, R13, R12 | 0.040 |
| D | H, T | R14, R1, R13, R12 | 0.079 |
| F | $HO_2$, $H_2O_2$, T | R14, R13, **R49**, R12 | 0.145 |
| G | $HO_2$, $H_2O_2$, T | R14, R13, **R49**, R12 | 0.328 |
| H | $NH_2$, $H_2O_2$, T | R14, R1, R13, **R49**, R12 | 0.714 |



**Fig. 15 — Time histories of pressure at the right boundary of different initial temperatures. (a) $a_{H_2} = 0.9$, and (b) $a_{H_2} = 0.1$.**
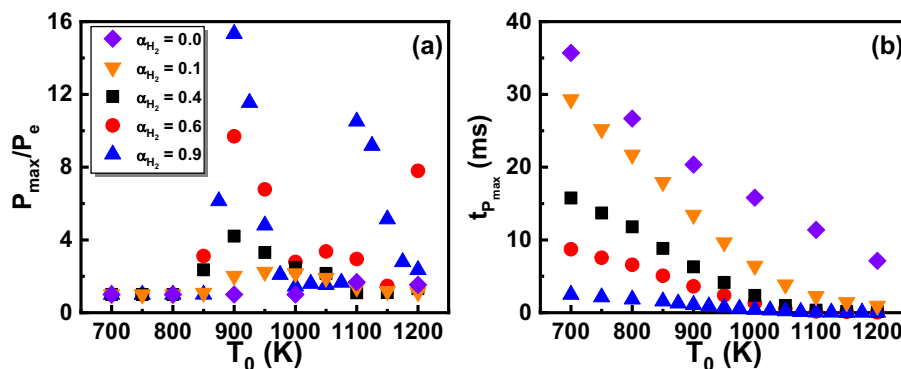
**Fig. 16** — Changes of (a) knocking intensity and (b) timing with initial end-gas temperature. Initial $H_2$ content is 0.0, 0.1, 0.4, 0.6, and 0.9, respectively.

process is smaller than that of homogeneous ignition (see Fig. 3). This is because the end-gas is disturbed by pressure wave and continuously compressed by the propagating flame front. Therefore, one can conclude that the controlling mechanisms of end-gas near the reactor wall during end-gas autoignition are generally similar to those from homogeneous ignition, but the pressure wave and propagating flame front can reduce the ignition delay as well as the proportion of thermal runaway process.

*Knocking intensity and timing*

Knocking intensity can be quantified from the evolution of the pressure oscillations near the reactor wall. A normalized maximum pressure, $P_{KI} = \frac{P_{max}}{P_e}$ [31,37], is introduced to measure the knocking intensity. Here $P_{max}$ and $P_e$ are the first peak pressure and equilibrium pressure obtained from the pressure history, respectively. Note that $P_{KI} = 1$ indicates the knocking-free combustion, and higher $P_{KI}$ (>1) corresponds to stronger knocking combustion. Besides, the knocking timing $t_{P_{max}}$ is also introduced to denote the instant when the pressure reaches its maximum.

Fig. 15 shows the time histories of pressure extracted from the reactor wall (probe location 4.0 cm). The initial hydrogen contents are $a_{H_2} = 0.9$ and 0.1, respectively. The corresponding changes of knocking intensity and timing are shown in Fig. 16. It is seen from Fig. 15(a) that, the near-wall pressure increases slowly at early stage, caused by the pressure wave disturbance. When the initial temperatures are 700 and 800 K, no pulsed pressure rises are observed, the corresponding $P_{KI}$ is close to 1, as seen from Fig. 16(a). They are knocking-free combustion (e.g., case A in Section 3.2). With increased initial temperature, the end-gas reactivity is enhanced, pressure peaks near the reactor wall are detected, caused by end-gas autoignition and/or detonation development (e.g., cases B – D). They correspond to knocking combustion, and the corresponding $P_{KI}$ is larger than 1 (see Fig. 16(a)). After reaching the peak, the pressure decreases and begins oscillating.

When the hydrogen mole ratio is 0.1, the initial temperatures of knocking-free combustion are less than 800 K (e.g., case E), which can be confirmed by the corresponding $P_{KI}$ (see Fig. 16(a)). For higher initial temperatures, knocking

combustion happens (e.g., 900 K, case F). Compared with the results in Fig. 15(a), the pressure oscillations in Fig. 15(b) are generally weaker, due to higher ammonia mole ratio and hence lower reactivity. Moreover, the higher initial temperature does not always lead to a higher $P_{KI}$, which can be found in both Fig. 16(a) and (b). For instance, the $P_{KI}$ of 950 K (4.8) is lower than that of 900 K (15.3) for $a_{H_2} = 0.9$ and the $P_{KI}$ of 1000 K (2.1) is lower than that of 950 K (2.2) for $a_{H_2} = 0.1$. This is also found in 1D simulations of stoichiometric hydrogen/air and n-heptane/air end-gas autoignition performed by Pan et al. [28,37]. This is because $P_{KI}$ is not only determined by the chemical reactivity in end-gas, but also affected by the interactions of flame propagation, pressure wave disturbance and end-gas combustion mode.

Besides, Fig. 16 also shows the changes of knocking intensity and timing of other three initial hydrogen contents, i.e., $a_{H_2} = 0$, 0.4, and 0.6. In general, the lower hydrogen mole ratio $a_{H_2}$, the weaker end-gas reactivity. Nonetheless, it is seen from Fig. 16(a) that, similar with the effects of initial temperature, higher $a_{H_2}$ does not always lead to a higher $P_{KI}$. For instance, the $P_{KI}$ of $a_{H_2} = 0.6$ (6.8) is higher than that of $a_{H_2} = 0.9$ (4.8) for 950 K. Besides, see from Fig. 16(b), knocking timing monotonically decreases with higher initial temperature and higher $a_{H_2}$.

## Conclusions

End-gas autoignition and detonation development in ammonia/hydrogen/air mixtures in a confined reactor is studied through detailed numerical simulations. One-dimensional planar confined chamber filled with $NH_3$/$H_2$/air mixtures is studied. Various initial end-gas temperatures ($T_0$) and hydrogen concentrations ($a_{H_2}$) in the binary fuels are considered.

Homogeneous ignition of stoichiometric $NH_3$/$H_2$/air mixtures is firstly calculated. The results show that $H_2$ addition significantly promotes autoignition. Beyond a critical value of $a_{H_2}$ (about 0.15), the dependence of ignition delay on hydrogen mole ratios $a_{H_2}$ is gradually reduced. For $NH_3$/air mixtures and $NH_3$/$H_2$/air mixtures with low hydrogen mole ratios, $NH_2$ and $H_2NO$ are most important nitrogen-containing species, and R49 ($NH_2$+NO<=>$N_2$+$H_2O$) is a crucial reaction during thermal runaway process, based on the chemical explosive mode

analysis. When the hydrogen mole ratio is high (e.g., $a_{H_2} = 0.9$), the nitrogen-containing species and reactions on the chemical explosive mode becomes less important.

Then a series of 1D detailed simulations is carried out. Based on the simulation results, three end-gas autoignition and combustion modes are observed, including forcibly ignited flame propagation, autoignition (no detonation), and detonation development. Knocking is not observed when $T_0$ is less than or equal to 800 K. It is seen that combustion of $NH_3$/$H_2$/air end-gas occurs when the initial temperature is above 800 K. Furthermore, end-gas autoignition can be observed when $a_{H_2}$ is less than or equal to 0.2. When the hydrogen mole fraction is greater than 0.2, besides autoignition, detonation in the end-gas can be initiated and develop under some favourable conditions. Moreover, when $a_{H_2} > 0.7$, detonation is always present when $T_0 > 800$ K.

Thermochemical state evolutions near the reaction front (i.e., flame front, autoignition front, and detonation front) and the reactor wall are revealed with chemical explosive mode analysis. It is found that the flame front in ammonia/hydrogen blend fuels is controlled by both thermal runaway and chemical runaway, autoignition front by thermal runaway, and detonation front mainly by chemical runaway. The controlling mechanisms at the position of autoignition initiation are generally like those from homogeneous ignition, but the pressure wave and/or propagating flame front can reduce the ignition delay as well as the proportion of thermal runaway process.

Finally, through the changes of knocking intensity and timing of different thermochemical conditions, a higher initial temperature or a higher $H_2$ content does not always lead to a higher knocking intensity. The knocking timing decreases with end-gas reactivity, such as higher initial temperature or higher $H_2$ content.

## Declaration of competing interest

The authors declare that they have no known competing financial interests or personal relationships that could have appeared to influence the work reported in this paper.

## Acknowledgement

## Appendix A. Supplementary data

Supplementary data to this article can be found online at https://doi.org/10.1016/j.ijhydene.2021.12.181.

REFERENCES

[1] Zamfirescu C, Dincer I. Ammonia as a green fuel and hydrogen source for vehicular applications. Fuel Process Technol 2009;90:729–37.

[2] Morgan E, Manwell J, McGowan J. Wind-powered ammonia fuel production for remote islands: a case study. Renew Energy 2014;72:51–61.

[3] Yapicioglu A, Dincer I. A review on clean ammonia as a potential fuel for power generators. Renew Sustain Energy Rev 2019;103:96–108.

[4] Kobayashi H, Hayakawa A, Somarathne KDKA, Okafor EC. Science and technology of ammonia combustion. Proc Combust Inst 2019;37:109–33.

[5] Valera-Medina A, Xiao H, Owen-Jones M, David WIF, Bowen PJ. Ammonia for power. Prog Energy Combust Sci 2018;69:63–102.

[6] Jing Q, Huang J, Liu Q, Wang D, Liu C. The flame propagation characteristics and detonation parameters of ammonia/oxygen in a large-scale horizontal tube: as a carbon-free fuel and hydrogen-energy carrier. Int J Hydrogen Energy 2021;46:19158–70.

[7] Kim HK, Ku JW, Ahn YJ, Kim YH, Kwon OC. Effects of O2 enrichment on NH3/air flame propagation and emissions. Int J Hydrogen Energy 2021;46:23916–26.

[8] Nozari H, Karabeyoǧlu A. Numerical study of combustion characteristics of ammonia as a renewable fuel and establishment of reduced reaction mechanisms. Fuel 2015;159:223–33.

[9] Kurata O, Iki N, Matsunuma T, Inoue T, Tsujimura T, Furutani H, et al. Performances and emission characteristics of NH3-air and NH3-CH4-air combustion gas-turbine power generations. Proc Combust Inst 2017;36:3351–9.

[10] Frigo S, Gentili R. Analysis of the behaviour of a 4-stroke Si engine fuelled with ammonia and hydrogen. Int J Hydrogen Energy 2013;38:1607–15.

[11] Dai L, Gersen S, Glarborg P, Levinsky H, Mokhov A. Experimental and numerical analysis of the autoignition behavior of NH3 and NH3/H2 mixtures at high pressure. Combust Flame 2020;215:134–44.

[12] Chen J, Jiang X, Qin X, Huang Z. Effect of hydrogen blending on the high temperature auto-ignition of ammonia at elevated pressure. Fuel 2021;287:119563.

[13] Issayev G, Giri BR, Elbaz AM, Shrestha KP, Mauss F, Roberts WL, et al. Combustion behavior of ammonia blended with diethyl ether. Proc Combust Inst 2021;38:499–506.

[14] Zhu R, Zhao M, Zhang H. Numerical simulation of flame acceleration and deflagration-to-detonation transition in ammonia-hydrogen–oxygen mixtures. Int J Hydrogen Energy 2021;46:1273–87.

[15] Lee JH, Lee SI, Kwon OC. Effects of ammonia substitution on hydrogen/air flame propagation and emissions. Int J Hydrogen Energy 2010;35:11332–41.

[16] Wang D, Ji C, Wang S, Yang J, Wang Z. Numerical study of the premixed ammonia-hydrogen combustion under engine-relevant conditions. Int J Hydrogen Energy 2021;46:2667–83.

[17] Grogan KP, Scott Goldsborough S, Ihme M. Ignition regimes in rapid compression machines. Combust Flame 2015;162:3071–80.

[18] Rudloff J, Zaccardi JM, Richard S, Anderlohr JM. Analysis of pre-ignition in highly charged SI engines: emphasis on the auto-ignition mode. Proc Combust Inst 2013;34:2959–67.

[19] Dahnz C, Spicher U. Irregular combustion in supercharged spark ignition engines - pre-ignition and other phenomena. Int J Engine Res 2010;11:485–98.

[20] Peters N, Kerschgens B, Paczko G. Super-knock prediction using a refined theory of turbulence. SAE Int J Engines 2013;6:953—67.

[21] Kurtz MD, Regele JD. Acoustic timescale characterisation of a one-dimensional model hot spot. Combust Theor Model 2014;18:532—51.

[22] Wang Z, Liu H, Reitz RD. Knocking combustion in spark-ignition engines. Prog Energy Combust Sci 2017;61:78—112.

[23] Qi Y, Wang Z, Wang J, He X. Effects of thermodynamic conditions on the end gas combustion mode associated with engine knock. Combust Flame 2014;162:4119—28.

[24] Kawahara N, Tomita E, Sakata Y. Auto-ignited kernels during knocking combustion in a spark-ignition engine. Proc Combust Inst 2007;31:2999—3006.

[25] Zhou L, Li K, Zhao J, Zhang X, Wei H. Experimental observation of end-gas autoignition and developing detonation in a confined space using gasoline fuel. Combust Flame 2020;222:1—4.

[26] Wei H, Zhang X, Zeng H, Deiterding R, Pan J, Zhou L. Mechanism of end-gas autoignition induced by flame-pressure interactions in confined space. Phys Fluids 2019;31:076106.

[27] Wang Z, Wang Y, Reitz RD. Pressure oscillation and chemical kinetics coupling during knock processes in gasoline engine combustion. Energy Fuel 2012;26:7107—19.

[28] Pan J, Shu G, Zhao P, Wei H, Chen Z. Interactions of flame propagation, auto-ignition and pressure wave during knocking combustion. Combust Flame 2016;164:319—28.

[29] Luong MB, Desai S, Hernández Pérez FE, Sankaran R, Johansson B, Im HG. A statistical analysis of developing knock intensity in a mixture with temperature inhomogeneities. Proc Combust Inst 2020. https://doi.org/10.1016/j.proci.2020.05.044.

[30] Morii Y, Dubey AK, Nakamura H, Maruta K. Two-dimensional laboratory-scale DNS for knocking experiment using n-heptane at engine-like condition. Combust Flame 2021;223:330—6.

[31] Terashima H, Koshi M. Mechanisms of strong pressure wave generation in end-gas autoignition during knocking combustion. Combust Flame 2015;162:1944—56.

[32] Terashima H, Matsugi A, Koshi M. Origin and reactivity of hot-spots in end-gas autoignition with effects of negative temperature coefficients: relevance to pressure wave developments. Combust Flame 2017;184:324—34.

[33] Terashima H, Matsugi A, Koshi M. End-gas autoignition behaviors under pressure wave disturbance. Combust Flame 2019;203:204—16.

[34] Terashima H, Nakamura H, Matsugi A, Koshi M. Role of low-temperature oxidation in non-uniform end-gas autoignition and strong pressure wave generation. Combust Flame 2021;223:181—91.

[35] Yu H, Chen Z. End-gas autoignition and detonation development in a closed chamber. Combust Flame 2015;162:4102—11.

[36] Yu H, Qi C, Chen Z. Effects of flame propagation speed and chamber size on end-gas autoignition. Proc Combust Inst 2017;36:3533—41.

[37] Pan J, Wei H, Shu G, Chen R. Effect of pressure wave disturbance on auto-ignition mode transition and knocking intensity under enclosed conditions. Combust Flame 2017;185:63—74.

[38] Manias DM, Patsatzis DG, Kyritsis DC, Goussis DA. NH3 vs. CH4 autoignition: a comparison of chemical dynamics. Combust Theor Model 2021:1—22.

[39] Bradley D, Lawes M, Mansour MS. Correlation of turbulent burning velocities of ethanol-air, measured in a fan-stirred bomb up to 1.2MPa. Combust Flame 2011;158:123—38.

[40] Bates L, Bradley D, Paczko G, Peters N. Engine hot spots: modes of auto-ignition and reaction propagation. Combust Flame 2016;166:80—5.

[41] Chen Z, Burke MP, Ju Y. Effects of Lewis number and ignition energy on the determination of laminar flame speed using propagating spherical flames. Proc Combust Inst 2009;32:1253—60.

[42] Chen Z. Effects of radiation and compression on propagating spherical flames of methane/air mixtures near the lean flammability limit. Combust Flame 2010;157:2267—76.

[43] Chen Z. Effects of hydrogen addition on the propagation of spherical methane/air flames: a computational study. Int J Hydrogen Energy 2009;34:6558—67.

[44] Li Z, Han W, Liu D, Chen Z. Laminar flame propagation and ignition properties of premixed iso-octane/air with hydrogen addition. Fuel 2015;158:443—50.

[45] Dai P, Chen Z. Supersonic reaction front propagation initiated by a hot spot in n-heptane/air mixture with multistage ignition. Combust Flame 2015;162:4183—93.

[46] Yu Z, Zhang H, Dai P. Autoignition and detonation development induced by temperature gradient in n-C7H16/air/H2O mixtures. Phys Fluids 2021;33:17111.

[47] Dai P, Qi C, Chen Z. Effects of initial temperature on autoignition and detonation development in dimethyl ether/air mixtures with temperature gradient. Proc Combust Inst 2017;36:3643—50.

[48] Sun M, Takayama K. Conservative smoothing on an adaptive quadrilateral grid. J Comput Phys 1999;150:143—80.

[49] Liberman MA, Ivanov MF, Valiev DM, Eriksson LE. Hot spot formation by the propagating flame and the influence of EGR on knock occurrence in si engines. Combust Sci Technol 2006;178:1613—47.

[50] Song Y, Hashemi H, Christensen JM, Zou C, Marshall P, Glarborg P. Ammonia oxidation at high pressure and intermediate temperatures. Fuel 2016;181:358—65.

[51] Otomo J, Koshi M, Mitsumori T, Iwasaki H, Yamada K. Chemical kinetic modeling of ammonia oxidation with improved reaction mechanism for ammonia/air and ammonia/hydrogen/air combustion. Int J Hydrogen Energy 2018;43:3004—14.

[52] Lu TF, Yoo CS, Chen JH, Law CK. Three-dimensional direct numerical simulation of a turbulent lifted hydrogen jet flame in heated coflow: a chemical explosive mode analysis. J Fluid Mech 2010;652:45—64.

[53] Goussis DA, Im HG, Najm HN, Paolucci S, Valorani M. The origin of CEMA and its relation to CSP. Combust Flame 2021;227:396—401.

[54] Luo Z, Yoo CS, Richardson ES, Chen JH, Law CK, Lu T. Chemical explosive mode analysis for a turbulent lifted ethylene jet flame in highly-heated coflow. Combust Flame 2012;159:265—74.

[55] Shan R, Yoo CS, Chen JH, Lu T. Computational diagnostics for n-heptane flames with chemical explosive mode analysis. Combust Flame 2012;159:3119—27.

[56] Wu W, Piao Y, Xie Q, Ren Z. Flame diagnostics with a conservative representation of chemical explosive mode analysis. AIAA J 2019;57:1355—63.

[57] Zhao M, Ren Z, Zhang H. Pulsating detonative combustion in n-heptane/air mixtures under off-stoichiometric conditions. Combust Flame 2021;226:285—301.

[58] Jaravel T, Dounia O, Malé Q, Vermorel O. Deflagration to detonation transition in fast flames and tracking with chemical explosive mode analysis. Proc Combust Inst 2021;38:3529—36.

[59] He X, Shu B, Nascimento D, Moshammer K, Costa M, Fernandes RX. Auto-ignition kinetics of ammonia and ammonia/hydrogen mixtures at intermediate temperatures and high pressures. Combust Flame 2019;206:189—200.

[60] Glassman I, Yetter RA, Glumac NG. Combustion. Academic press; 2014.

[61] Jiménez C, Quinard J, Graña-Otero J, Schmidt H, Searby G. Unsteady response of hydrogen and methane flames to pressure waves. Combust Flame 2012;159:1894—908.

[62] Zhao J, Zhou L, Zhang X, Li K, Wei H. Experimental investigation of combustion modes and transition mechanism in confined combustion chamber. Combust Flame 2021;230:111451.

[63] Zhao J, Zhou L, Li K, Zhang X, Pan J, Chen R, et al. Effect of diluent gases on end-gas autoignition and combustion modes in a confined space. Combust Flame 2020;222:48—60.

[64] He X, Qi Y, Wang Z, Wang J, Shuai S, Tao L. Visualization of the mode shapes of pressure oscillation in a cylindrical cavity. Combust Sci Technol 2015;187:1610—9.